RESEARCH ARTICLE | MARCH 22 2024

Deicing and status characteristics of dual-side pulsed surface dielectric barrier discharge

Bangfa Peng (彭邦发) ; Jie Li (李杰) ; Nan Jiang (姜楠) ; Yan Jiang (姜岩); Zhanqing Chen (陈占清) ; Zhipeng Lei (雷志鹏) ; Jiancheng Song (宋建成)

Physics of Fluids 36, 037144 (2024)
https://doi.org/10.1063/5.0191124

Physics of Fluids ARTICLE pubs.aip.org/aip/pof

Deicing and status characteristics of dual-side pulsed surface dielectric barrier discharge

Cite as: Phys. Fluids **36**, 037144 (2024); doi: 10.1063/5.0191124
Submitted: 11 December 2023 · Accepted: 5 March 2024 ·
Published Online: 22 March 2024

Bangfa Peng (彭邦发),[1] Jie Li (李杰),[2,a)] Nan Jiang (姜楠),[2] Yan Jiang (姜岩),[2] Zhanqing Chen (陈占清),[1] Zhipeng Lei (雷志鹏),[1] and Jiancheng Song (宋建成)[1]

AFFILIATIONS

[1]Shanxi Key Laboratory of Mining Electrical Equipment and Intelligent Control, College of Electrical and Power Engineering, Taiyuan University of Technology, Taiyuan, Shanxi 030024, China
[2]School of Electrical Engineering, Dalian University of Technology, Dalian 116024, People's Republic of China

[a)]Author to whom correspondence should be addressed: lijie@dlut.edu.cn

ABSTRACT

The deicing process and its status characteristics of dual-side pulsed surface dielectric barrier discharge (SDBD) are studied via electro-optical diagnostics, thermal properties, and numerical simulation. Experimental results show that the dual-side pulsed SDBD can remove the glaze ice compared to the traditional pulsed SDBD under the applied pulse voltage of 8 kV and a pulse frequency of 1 kHz. The maximal temperature of dual-side pulsed SDBD reaches 39.5 °C under the discharge time of 800 s, while the maximal temperature of traditional pulsed SDBD is still below ice point about −7.8 °C. Surface temperatures of dual-side pulsed SDBD demonstrate that the SDBD with a gap of 1 mm possesses prospects in deicing. The maximal surface temperature reaches 37.1 °C under the pulse of 8 kV after the discharge time of 90 s. Focusing on the thermal effect, a two-dimensional plasma fluid model is implemented, and the results also indicate that the dual-side pulsed SDBD with a gap of 1 mm produces a highest heat density among the three different configurations. Comparing the spatial-temporal evolutions of plasma on both dielectric sides, primary positive streamer has a longer propagation length of 8.6 mm than the secondary negative streamer, the primary negative streamer, and the secondary positive streamer, which induces a long heat covered area. Four stages of deicing process are analyzed through a series of electrical parameters under different covered ice conditions.

NOMENCLATURE

AC	Alternating current
D_i	Diffusion coefficient of species, m^2/s
D_ϵ	Diffusion coefficient of mean electron energy, m^2/s
GE	Grounded electrode
HV	High voltage
LMEA	Local mean energy approximation
N_{charge}	Number of charged species
N_{total}	Number of all species
n_i	Species number density, m^{-3}
PASSKEy	Parallel Streamer Solver with Kinetics
q_i	Charge, C
SDBD	Surface dielectric barrier discharge
S_i	Source of species generation and consumption, 1/(m^3 s)
S_{ph}	Photoionization sources, 1/(m^3 s)
T_{gas}	Gas temperature, K
T_e	Electron temperature, K
t	Time, s
2 D	Two-dimensional

Greek symbols

$\boldsymbol{\Gamma}_i$	Species flux, 1/(m^2 s)
$\boldsymbol{\Gamma}_\epsilon$	Power lost by the electrons in collisions, eV/s
δ_s	Kronecker delta function
ε_r	Relative permittivity
ε_0	Vacuum permittivity
μ_i	Mobility coefficient of species, m^2/V s
μ_ϵ	Mobility coefficient of mean electron energy, m^2/V s
ρ_c	Charge density on dielectric surface, C/m^2
Φ	Electrical potential, V

Subscripts

e	Electron
i	Species
m	Mean electron energy, eV

I. INTRODUCTION

Ice accretion on the surfaces of aircrafts and wind turbines may be occurring, when they operate in low temperature and high humidity environment, which has been widely recognized as a significant safety hazard.[1–3] The ice formed on the equipment's surface will dramatically alter the original aerodynamic characteristics, which can affect its normal operation.[4,5] Although a series of strategies has been proposed for icing mitigation, various drawbacks are still far from being completely resolved. For example, the electrical heating and gas heating can make the surface temperature above the freezing point of water, but it requires much energy.[6] The aqueous solution may cause environmental pollutions to soil and water.[7] The hydrophobic and ice phobic coating material has been shown that it is inefficient and disabled after long time operation.[8] Moreover, the mechanical deicing system may damage the material and structure.[9] As a result, it is desperately desirable to develop a novel deicing method characterized with low power requirement, environmentally friendly, and simple design.

Discharge plasma can be generated by the accelerated electrons collision with neutral species under the effect of applied electric field, which induces the ionization, excitation, dissociation, and related reaction processes.[10,11] Physical and chemical effects are also formed with the plasma generation, which have been attracted attention in different application fields, including environmental protection,[12] flow control,[13] assisted combustion,[14] energy conversion,[15] and biomedicine.[16] In recent years, the discharge plasma has been developed to become a novel anti-/deicing technique based on its thermal effect[17–20] or shock wave.[21–23] The feasibility of the anti-icing and deicing via surface dielectric barrier discharge (SDBD) is first demonstrated by Meng *et al.* in the year of 2016.[24] Then, a series of experiments indicate that the heat produced by the SDBD possesses better anti-/deicing performance than the traditional electric heating film effect due to the extended heated domain in air.[25] Through the modulated voltage waveform,[26] it is believed that the modulated alternating current (AC) SDBD possesses an better anti-/deicing performance than that of the continuous actuation mode under the same power input due to the high instantaneous voltage. Compared to the AC power supply in SDBD, the nanosecond pulse shows a better deicing prospect under the same deposited energy due to the large heating region.[27] To improve the deicing performances, a "stream-wise plasma heat knife" configuration driven by nanosecond pulse is proposed for anti-icing. The result shows that the novel configuration has a better performance than the traditional spanwise actuator array.[28] SDBD combining with superhydrophobic coatings reveals that the instantaneous energy utilization rate of the coated actuator at 60 s of deicing process is about 54% higher compared to the uncoated actuator.[29] Moreover, the microelectromechanical systems present a clear advantage for anti-icing than that of traditional SDBD.[30] For the mechanism of deicing, an ice bead accumulated on dielectric surface found that the ice melted faster on the side close to the high voltage (HV) electrode in AC-DBD plasma actuator.[31] It also found that the thermal effects and the aerodynamic force play dominant role on the mechanisms of nanosecond pulsed SDBD deicing.[32] Furthermore, the DBD-based plasma analyzed by numerical simulation indicates that the direct fast gas heating energy transfer from gas to ice/water accumulated on the surface in each duty cycle plays a key role on icing prevention.[33] According to the shock wave effect, a HV electrode and a grounded electrode (GE) are placed inside the ice, which can induce a pulsed spark discharge and form a strong shock wave to break the covered glaze ice.[34] Furthermore, a shock wave generated by the plasma synthetic jet also can induce the ice-breaking.[35,36] Despite the low energy requirement for the ice-breaking based on shock wave, there is a limitation in the application field. For example, the broken ice may directly enter the aircraft engine and result in fatal damage. According to these works, it is believed that the SDBD based on thermal effect shows a prospect for application in deicing.

Generally, there are three different ice accretion models corresponding to rime ice, mixed ice, and glaze ice. In particular, the glaze ice is considered to be the most dangerous for normal operation, which is difficult to remove due to its strong adhesion ability.[37] When the traditional pulsed SDBD is covered by glaze ice, the plasma cannot be produced on the HV electrode side due to the fact that there is no enough air inside the ice, and the ice plays a role of dielectric.[38] As a result, the glaze ice covered on traditional pulsed SDBD cannot be removed effectively. Fortunately, a dual-side pulsed SDBD characterized with exposed GE is proposed to address the problem of traditional SDBD. When the HV electrode is covered with glaze ice, the plasma can be produced on the GE side. According to the heat generation and conduction from the GE side, the glaze ice is melted and forms an air gap. As a result, the plasma can be induced on the HV electrode side, and the plasma can interact with the glaze ice directly. Therefore, the covered glaze ice can be melted effectively and rapidly.

Plasma numerical simulation is a suitable method to describe the micro-characteristics of single pulse discharge including the species evolution and heat generation, which is difficult to be measured via the experiments.[39] Although the three-dimension model should have a deep insight into the visual physical phenomenon, a large computational burden should be addressed.[40] Therefore, a series of two-dimensional (2D) numerical models is implemented to reveal some puzzles of the discharge process, which has shown prospect in revealing physical mechanism of plasma.[41] For example, a pulsed pin-to-plate discharge characterized with primary and secondary streamers is studied in the 2D plasma fluid model.[42] The various discharge modes of surface discharge and volume discharge in the packed-bed discharge are also analyzed via the fluid model.[43] In the SDBD configuration, the traditional SDBD configuration with plasma evolution has been studied.[44] Furthermore, the heat generation and distribution of dual-side pulsed SDBD should be studied to analyze its effect on the deicing, which can contribute to improving the selection of SDBD configuration.

In the present work, the experimental and numerical methodologies are introduced in Sec. II. In Sec. III, the deicing process and thermal variation of the traditional pulsed SDBD and dual-side pulsed SDBD are analyzed. In addition, spatial-temporal evolutions of surface temperature for the dual-side pulsed SDBD with the three different gaps are measured to determine the optimal configuration. Then, a 2D plasma fluid model is built to reveal the thermal effect and plasma process on the HV electrode and GE sides. Furthermore, the deicing process and its status characteristics are discussed according to the electrical properties, and methods of single and double phase analysis. Finally, the main features and future works are summarized in Sec. IV.

II. EXPERIMENTAL AND NUMERICAL METHODOLOGIES

A. Experimental methodology

In order to have a deep insight into the plasma characteristics and deicing process by dual-side pulsed SDBD, a scheme of experimental setup is built, as presented in Fig. 1. A nanosecond pulsed generator (HVP-20P, Xi'an Smart Maple Electronic Technology Co. Ltd., China) is utilized to produce plasma. The electrical characteristics of applied voltage and discharge current are measured via a HV probe (Tektronix P6015A) and a current probe (Tektronix P6021A), respectively. An infrared imager (FOTRIC 222S) is utilized to monitor the spatial-temporal evolution of surface temperature for SDBD with a vertical distance of 20 cm. Also, a digital camera located at a vertical distance of 30 cm is used to record the plasma morphology, the deicing process, and the plasma interaction with ice. The detailed description of dual-side pulsed SDBD configuration is shown in Fig. 1(b). The configuration consists of a dielectric film arranged with an exposed HV electrode and an exposed GE on the two dielectric surfaces. The dielectric film is made of polyimide with a thickness of 0.25 mm. The HV electrode and GE are made of rectangular aluminum foils characterized with dimensions $x \times y \times z = 10 \times 60 \times 0.1$ mm. Furthermore, three gaps (−1, 0, and 1 mm) between the edge of HV electrode and the edge of GE are developed to analyze the thermal characteristics of different dual-side pulsed SDBD configurations. The covered glaze ice can be melted into water during the deicing process. Then, the air will enter the ice after the water flow out the dielectric surface. In order to analyze the effect of different phases on deicing status, the whole discharge region in HV electrode side is separated into different domains with a certain proportion (0%, 12.5%, 25%, 50%, 75%, and 100%) in Fig. 1(b). These current proportions can indicate the variation trend effectively. The different proportion in air–water mixture, air–ice mixture, and water–ice mixture can be developed to analyze the effect of phase proportion on plasma characteristics. For example, the proportion of water–ice mixture is set as 50%, which means that the half region is filled with water, and another region is filled with ice on the HV electrode side. The whole deicing process of pulsed SDBD is implemented inside a refrigerator [Fig. 1(c)], which is utilized to simulate the actual ambient temperature. Here, the glaze ice, as a most harmed ice type, is formed on the HV electrode surface. The glaze ice is prepared advance, a certain amount of water is put into the corresponding domain of the separated region, and then the whole configuration is placed into the refrigerator to form glaze ice with about 2 mm or 4 mm in thickness.

B. Numerical methodology

To get a deep understanding of the heat distribution in the dual-side SDBD configuration with three gaps (−1, 0, and 1 mm), a 2 D plasma fluid model is proposed. The plasma fluid model is implemented by an open source code of Parallel Streamer Solver with Kinetics (PASSKEy),[45] which has been verified by a series of experimental results, including plasma process, voltage–current characteristics, and electric field evolutions.[46] The detailed description of the simulation model can be seen in Refs. 46 and 47. Here, the drift-diffusion-reaction equations for species, the electron energy equation for mean electron energy, and Poisson's equations are shown as follows:[47]

$$\frac{\partial n_i}{\partial t} + \nabla \cdot \mathbf{\Gamma}_i = S_i + S_{ph}, \quad i = 1, 2, \ldots, N_{total}, \tag{1}$$

$$\mathbf{\Gamma}_i = -\left(\frac{q_i}{|q_i|}\right)\mu_i n_i \nabla\Phi - D_i \nabla n_i, \quad i = 1, 2, \ldots, N_{charge}, \tag{2}$$

$$\frac{\partial}{\partial t}(n_e \epsilon_m) + \nabla \cdot \mathbf{\Gamma}_\epsilon = \frac{q_i}{|q_i|}\Gamma_e \cdot \nabla\Phi - P(\epsilon_m), \tag{3}$$

$$\mathbf{\Gamma}_\epsilon = \mu_\epsilon n_e \epsilon_m \nabla\Phi - D_\epsilon \nabla(n_e \epsilon_m), \tag{4}$$

$$\nabla(\varepsilon_0 \varepsilon_r \nabla\Phi) = -\sum_{i=1}^{N_{charge}} q_i n_i - \rho_c \delta_s, \tag{5}$$

where n_i and $\mathbf{\Gamma}_i$ are the number density and species flux of species i, respectively. S_i indicates the source of species generation and consumption from the selected 40 reactions with 18 species (see Table I). For the selection of kinetic reactions, there are a large number of species collision reactions in air discharge plasma. The numerical model coupled with whole reaction will significantly consume more computational time. As a result, a reduced kinetic reaction scheme is selected based on the corresponding pre-simulation and published works. S_{ph} is the photoionization sources, which is calculated through the three-exponential Helmholtz model. Based on the photoionization, the surface streamer can be described more accurate.[48] q_i μ_i, D_i, μ_ϵ, and D_ϵ are the charge, mobility coefficient of species i, diffusion coefficient of species i, and rate coefficients of electron impact reactions represented as explicit functions of mean electron energy (ϵ_m) based on local mean energy approximation (LMEA), respectively. Φ and $P(\epsilon_m)$ are the

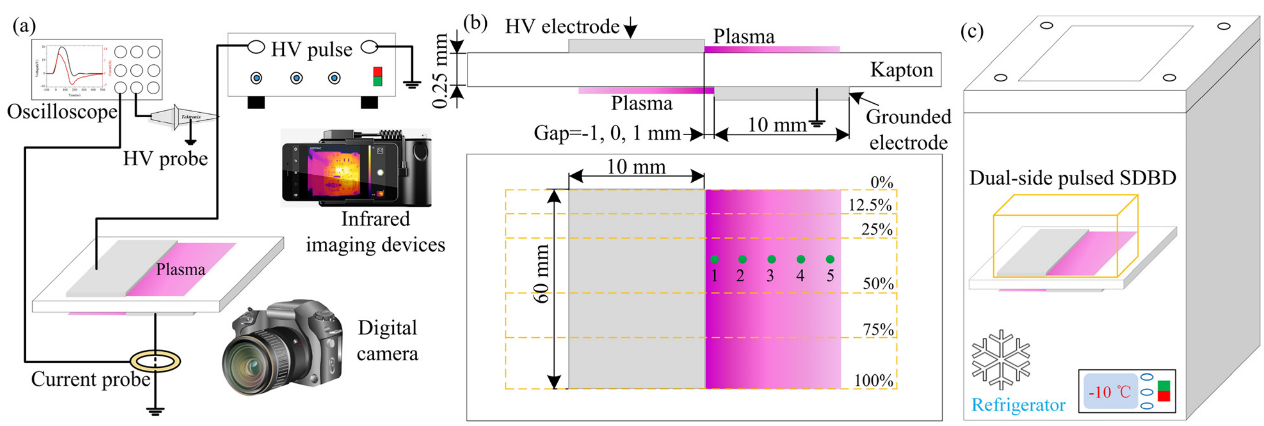

FIG. 1. Schematic diagram of experimental setup: (a) scheme of the dual-side pulsed SDBD, (b) detail configuration of dual-side pulsed SDBD and different proportion separation, and (c) deicing system.

TABLE I. Kinetic reaction scheme of the numerical model.

No.	Reaction	Rate constant	References
R1	$e + N_2 \rightarrow N_2^+ + e + e$	$f(\sigma, \varepsilon_m)$	49
R2	$e + O_2 \rightarrow O_2^+ + e + e$	$f(\sigma, \varepsilon_m)$	50
R3	$e + O_2 \rightarrow O^- + O$	$f(\sigma, \varepsilon_m)$	50
R4	$e + N_2 \rightarrow e + N_2(C^3\Pi_u)$	$f(\sigma, \varepsilon_m)$	49
R5	$e + O_2 \rightarrow e + O + O$	$f(\sigma, \varepsilon_m)$	50
R6	$e + O_2 \rightarrow e + O + O(^1D)$	$f(\sigma, \varepsilon_m)$	50
R7	$e + N_2 \rightarrow e + N_2(A^3\Sigma_u)$	$f(\sigma, \varepsilon_m)$	49
R8	$e + N_2 \rightarrow e + N_2(B^3\Pi_g)$	$f(\sigma, \varepsilon_m)$	49
R9	$N_2^+ + N_2 + N_2 \rightarrow N_4^+ + N_2$	5×10^{-29}	51
R10	$N_2^+ + N_2 + O_2 \rightarrow N_4^+ + O_2$	5×10^{-29}	51
R11	$N_4^+ + O_2 \rightarrow O_2^+ + N_2 + N_2$	2.5×10^{-10}	51
R12	$N_2^+ + O_2 \rightarrow O_2^+ + N_2$	$6 \times 10^{-11}(300/T_{gas})^{0.5}$	52
R13	$O_2^+ + N_2 + N_2 \rightarrow O_2^+N_2 + N_2$	$9 \times 10^{-31}(300/T_{gas})^2$	52
R14	$O_2^+N_2 + N_2 \rightarrow O_2^+ + N_2 + N_2$	4.3×10^{-10}	53
R15	$O_2^+N_2 + O_2 \rightarrow O_4^+ + N_2$	1×10^{-9}	53
R16	$O_2^+ + O_2 + N_2 \rightarrow O_4^+ + N_2$	$2.4 \times 10^{-30}(300/T_{gas})^{3.2}$	52
R17	$O_2^+ + O_2 + O_2 \rightarrow O_4^+ + O_2$	$2.4 \times 10^{-30}(300/T_{gas})^{3.2}$	52
R18	$e + O_4^+ \rightarrow O + O + O_2$	$1.4 \times 10^{-6}(300/T_e)^{0.5}$	51
R19	$e + O_2^+ \rightarrow O + O$	$2 \times 10^{-7}(300/T_e)$	51
R20	$e + O_2 + O_2 \rightarrow O_2^- + O_2$	$2 \times 10^{-29}(300/T_e)$	53
R21	$O_2^- + O_4^+ \rightarrow O_2 + O_2 + O_2$	1×10^{-7}	53
R22	$O_2^- + O_4^+ + N_2 \rightarrow O_2 + O_2 + O_2 + N_2$	$2 \times 10^{-25}(300/T_{gas})^{3.2}$	53
R23	$O_2^- + O_4^+ + O_2 \rightarrow O_2 + O_2 + O_2 + O_2$	$2 \times 10^{-25}(300/T_{gas})^{3.2}$	53
R24	$O_2^- + O_2^+ + N_2 \rightarrow O_2 + O_2 + N_2$	$2 \times 10^{-25}(300/T_{gas})^{3.2}$	53
R25	$O_2^- + O_2^+ + O_2 \rightarrow O_2 + O_2 + O_2$	$2 \times 10^{-25}(300/T_{gas})^{3.2}$	53
R26	$O^- + N_2^+ \rightarrow O + N + N$	1×10^{-7}	52
R27	$e + N_4^+ \rightarrow N_2 + N_2(C^3\Pi_u)$	$2 \times 10^{-6}(300/T_e)^{0.5}$	52
R28	$e + N_2^+ \rightarrow N + N$	$2.8 \times 10^{-7}(300/T_e)^{0.5}$	52
R29	$N_2(C^3\Pi_u) \rightarrow N_2(B^3\Pi_g) + h\upsilon$	2.38×10^7	52
R30	$N_2(C^3\Pi_u) + N_2 \rightarrow N_2(B^3\Pi_g) + N_2$	0.13×10^{-10}	51
R31	$N_2(C^3\Pi_u) + O_2 \rightarrow N_2 + O + O(^1D)$	3×10^{-10}	51
R32	$N^+ + O_2 \rightarrow O_2^+ + N$	2.8×10^{-10}	52
R33	$O^+ + O_2 \rightarrow O_2^+ + O$	2×10^{-11}	54
R34	$O^- + O \rightarrow O_2 + e$	5×10^{-10}	52
R35	$O_2^- + O \rightarrow O_2 + O + e$	1.5×10^{-10}	52
R36	$N_2(A^3\Sigma_u) + O_2 \rightarrow N_2 + O + O$	$2.5 \times 10^{-12}(T_{gas}/300)^{0.5}$	51
R37	$N_2(B^3\Pi_g) + O_2 \rightarrow N_2 + O + O$	3×10^{-10}	51
R38	$N_2(B^3\Pi_g) + N_2 \rightarrow N_2(A^3\Sigma_u) + N_2$	1×10^{-11}	51
R39	$O(^1D) + O_2 \rightarrow O + O_2$	$3.3 \times 10^{-11}\exp(67/T_{gas})$	51
R40	$O(^1D) + N_2 \rightarrow O + N_2$	$1.8 \times 10^{-11}\exp(107/T_{gas})$	51

electrical potential and the power lost by the electrons in collisions, respectively. ε_0 and ε_r indicate the vacuum permittivity and relative permittivity, respectively. ρ_c and δ_s denote the charge density on dielectric surface and Kronecker delta function (equal to 1 on the plasma/dielectric interfaces), respectively. N_{total} and N_{charge} are the number of all species and charged species, respectively.

Rate constants are given in cm^{-6}, cm^{-3}, and s^{-1} for three-body reaction, two-body reaction, and single-body reaction, respectively. T_{gas} and T_e indicate the gas temperature and electron temperature with the unit of K, respectively. The rate constants of electron collision reaction (R1–R8) are calculated by BOLSIG+.[55]

A 2D computational domain with a length of 20 mm and a thickness of 5 mm for dual-side SDBD with a gap of 1 mm is shown in Fig. 2. The dielectric is set as 0.25 mm in thickness and a relative permittivity of 4. The HV electrode and GE located on the two dielectric surfaces are in the same dimension of $x \times y = 10 \times 0.1\ mm^2$. For the

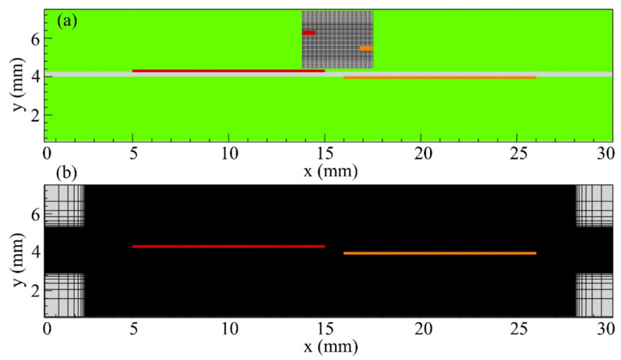

FIG. 2. Geometrical model: (a) computational domain and (b) meshes.

selection of mesh, a finer mesh has been adopted for the simulation, and it consumes more time. The results agree well with the current works. Considering the computing source and time, A finer mesh of 6 μm is used to discretize the domain around the surfaces of electrode and dielectric because of the large electric field and high species density. A coarse mesh of 15 μm is adopted to the other domain, which aims to decrease the computational resource. As a result, 691 564 meshes are formed in our model of dual-side SDBD. Suitable boundary conditions are required for the numerical simulation. The gas temperature and pressure are set as 300 K and 1 atm, respectively, which are consisting with experimental conditions. The initial electron density and electron energy are assumed to be 1×10^{10} m^{-3} and 0.5 eV, respectively. Furthermore, the pulse voltage for HV electrode is extracted from the oscilloscope and applied on the HV electrode.

III. RESULTS AND DISCUSSION

A. Comparison on the deicing of two pulsed SDBD configurations

To have a deep insight into the effect of discharge on GE side, a series of experiments including deicing images, plasma morphology, and voltage–current characteristics from two configurations of traditional pulsed SDBD and dual-side pulsed SDBD are presented in Fig. 3. It can be seen that there is no discharge in the traditional pulsed SDBD, when the HV electrode is covered by glaze ice [see Fig. 3(a)]. Therefore, the glaze ice is still covered on the surface of SDBD configuration. The reason is that there is no gap inside the covered glaze ice, and the glaze ice can be regarded as a dielectric.[38] As a result, the discharge is difficult to be ignited inside the glaze ice. Therefore, there is no heat generation in the absence of discharge, which is unable to melt the glaze ice. Fortunately, the dual-side pulsed SDBD can make an effective deicing. Because the plasma can be produced on the GE side, then, the generated heat will transfer into the HV electrode side through the dielectric. As a result, the covered glaze ice can be melted, and, thus, air gap will be formed around the edge of HV electrode. Also, when the ice is melted into the water, some water covered on the dielectric surface will inhibit the surface plasma. After the water run away, the air gap will enlarge, and the plasma can be generated. Under the effect of applied pulse voltage, the plasma can be induced from the HV electrode side [see Fig. 3(b)]. After that, the discharge plasma not only produced on the GE side but also generated on the HV electrode side. The generated plasma can act directly on the glaze ice, resulting in the ice melting around the HV electrode more effectively.

In order to have a further insight on the deicing process of two pulsed SDBD configurations, the electrical characteristics are analyzed, as shown in Fig. 4. In which, the temporal evolution of discharge power is calculated from the real-time measured voltage and current during the deicing process. Compared the discharge current and discharge power of these two pulsed SDBD configurations, the discharge power almost remains stable for the whole deicing process through the traditional pulsed SDBD. This phenomenon also indicates that the traditional pulsed SDBD is unable to realize deicing. Furthermore, the low discharge power is caused by the slight micro-discharge inside the covered ice. However, the discharge filaments are not sufficient for deicing due to the low energy input. It is due to the fact that the discharge is inhibited by the covered glaze ice in the absence of air gap. Therefore, the current measured by the probe is mainly consisting of displacement current.[56] As a result, the glaze ice is still covered on the surface of SDBD. However, the dual-side pulsed SDBD shows different changing rule. The discharge power remains unchanged at the early stage (before 100 s) because the plasma is only produced on the GE side. As the development of discharge, the covered ice on HV electrode is melted. As a result, the HV electrode exposed to the air, which can generate the plasma on the HV electrode side. The discharge power increases with the increase in plasma area of HV electrode side.

B. Temporal evolution of surface temperature during deicing process

The thermodynamic images and maximal temperature of deicing process for two pulsed SDBD configuration are shown in Figs. 5 and 6, respectively. To deal with the effect of light reflection from the electrode, the infrared imaging is obtained under the dark environment. The experimental results show that the maximal temperature is still below 0 °C (ice point) from 0 to 500 s in the traditional pulsed SDBD, which indicates that the traditional pulsed SDBD is unable to remove the ice. Because the traditional SDBD covered by the glaze ice does not possess an enough air gap, and the ice also plays a role of dielectric. As a result, the plasma is not easy to be produced, and the glaze ice is unable to be removed. For the dual-side pulsed SDBD, the maximal temperature increases into 39.5 °C with the discharge time of 800 s. It also can be noted that there is no plasma generation after the glaze ice covered the HV electrode side during the initial stage of deicing. The plasma is produced on the GE side when it is exposed to the air. Based on the fast gas heating of pulsed plasma in grounded side, the heat can be converted to the HV electrode side and melt the ice near the HV electrode. It also noted that a hot spot appears at the edge of HV electrode at the time of 100 s, which indicates that plasma is produced in this region and produces fast gas heating. As a result, the ice is melted, and the area of high temperature region increases with the time. According to the direct interaction of plasma, the covered ice can be melted quickly. As the ice melts, more plasma is generated in the HV electrode region.

C. Surface temperature distribution in the dual-side SDBD with three gaps

The heat generated by the dual-side pulsed SDBD plays a critical role in the deicing performance. Furthermore, it is important to make high temperature and large heat region on the HV electrode side,

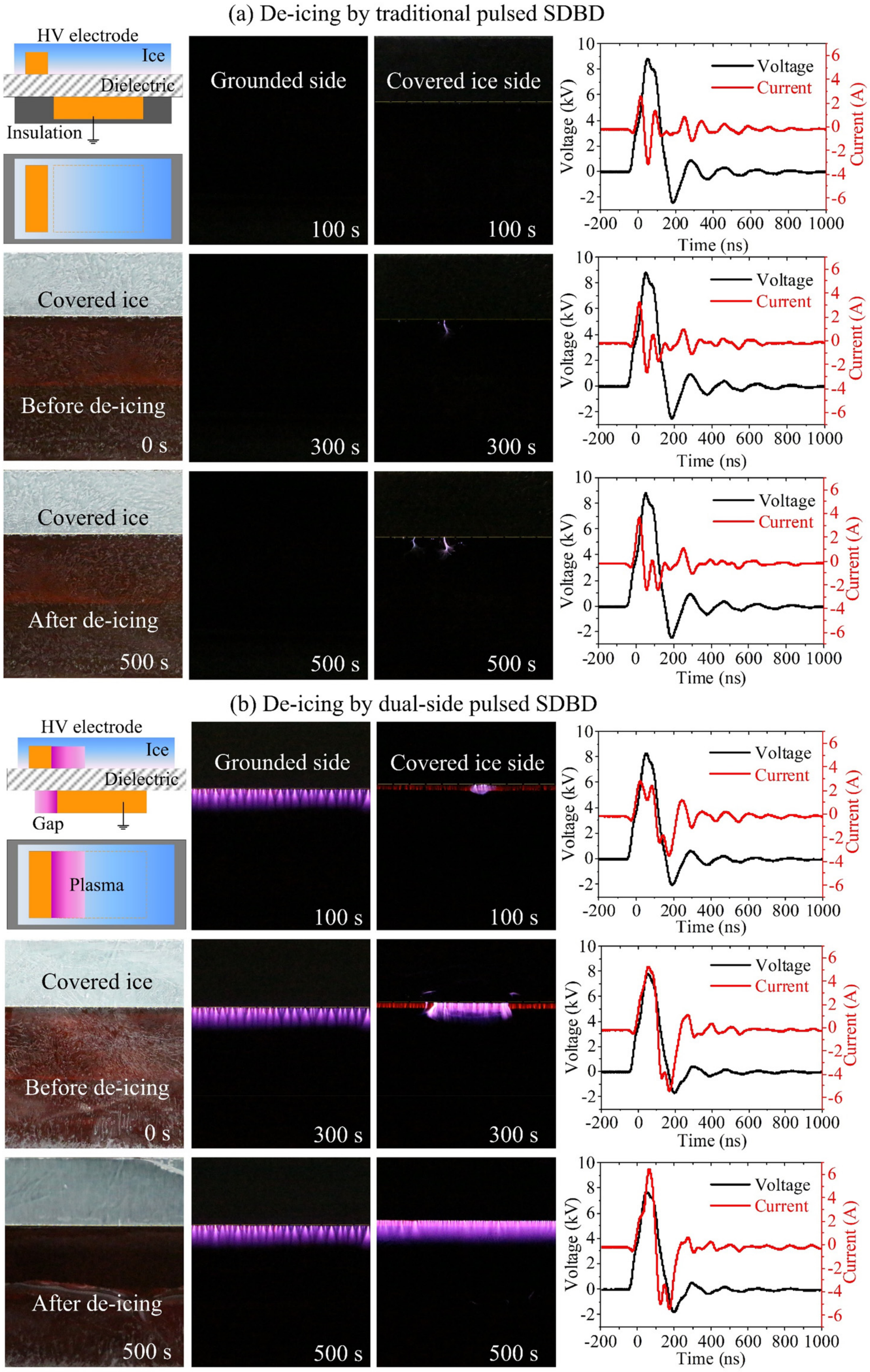

FIG. 3. Comparison of deicing process, plasma morphology, and electrical characteristics at 8 kV and 1 kHz by (a) traditional pulsed SDBD and (b) dual-side pulsed SDBD.

which is favorable for melting the covered glazed ice. The surface temperature distributions of the dual-side pulsed SDBD with a gap of −1, 0, and 1 mm are shown in Fig. 7. From the results, it can be noted that the SDBD characterized with a 1 mm gap between the HV electrode and GE possesses a maximal temperature on the HV electrode side among the three different configurations. The reason is that the surface plasma produced on the GE side also can generate a fast gas heating[51] and transfer to the HV electrode side. In addition, a longer plasma

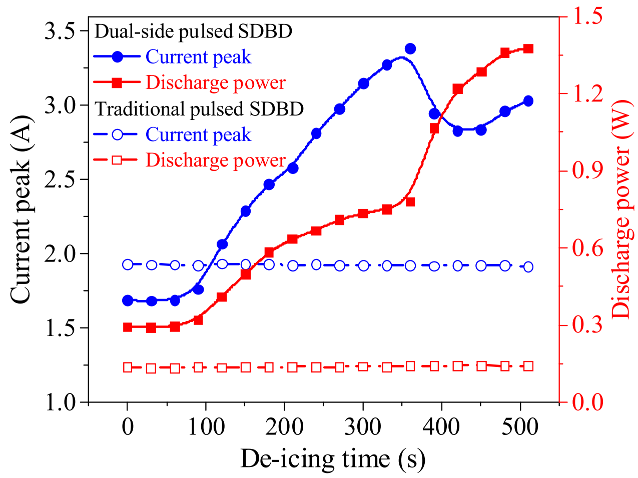

FIG. 4. Temporal evolution of current peak and discharge power in traditional pulsed SDBD and dual-side pulsed SDBD.

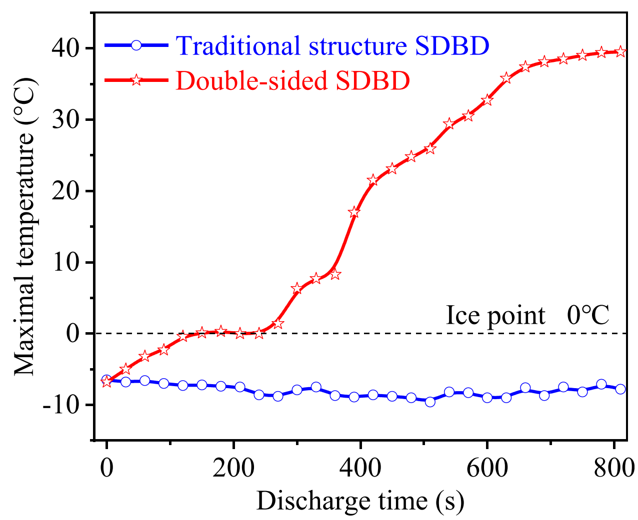

FIG. 6. Temporal evolution of maximal surface temperature during deicing process of the traditional pulsed SDBD and dual-side pulsed SDBD.

channel can be formed in the dual-side SDBD with 1 mm gap, which is favor for the heat generation (see Sec. III D in numerical simulation). Based on the thermal effect of plasma on the HV electrode and GE sides, a high temperature is obtained in the HV electrode region. It also shows that the temperature decreases along the streamer propagation direction. Because a high electric field strength is induced near the HV electrode, which is favorable to the ionization and excitation processes.[57] As a result, more heat is generated around the HV electrode.

The temporal evolution of temperature for five points along the HV electrode side is shown in Fig. 8. It can be seen that the temperature increases with the time and reaches a stable status. The reason is that more electrical energy is injected into the SDBD configuration through the fast gas heating of pulse discharge. Furthermore, the heat accumulation and heat dissipation achieve a dynamic equilibrium in the pulsed SDBD. The first point possesses a maximal temperature during the whole discharge process because of the strong ionization and excitation processes around the HV electrode domain.[58] The evolution of maximal temperature along the dielectric surface for three SDBD configurations under different applied pulse voltages is also studied and shown in Fig. 8. It can be noted that the double-side pulsed SDBD with a gap of 1 mm possesses a maximal temperature among the three SDBD configurations. The maximal temperature reaches 37.1 °C at the pulse voltage of 8 kV. Based on the aforementioned descriptions, the double-side pulsed SDBD with a gap of 1 mm is selected to deicing in our work due to its high surface temperature and large covered region.

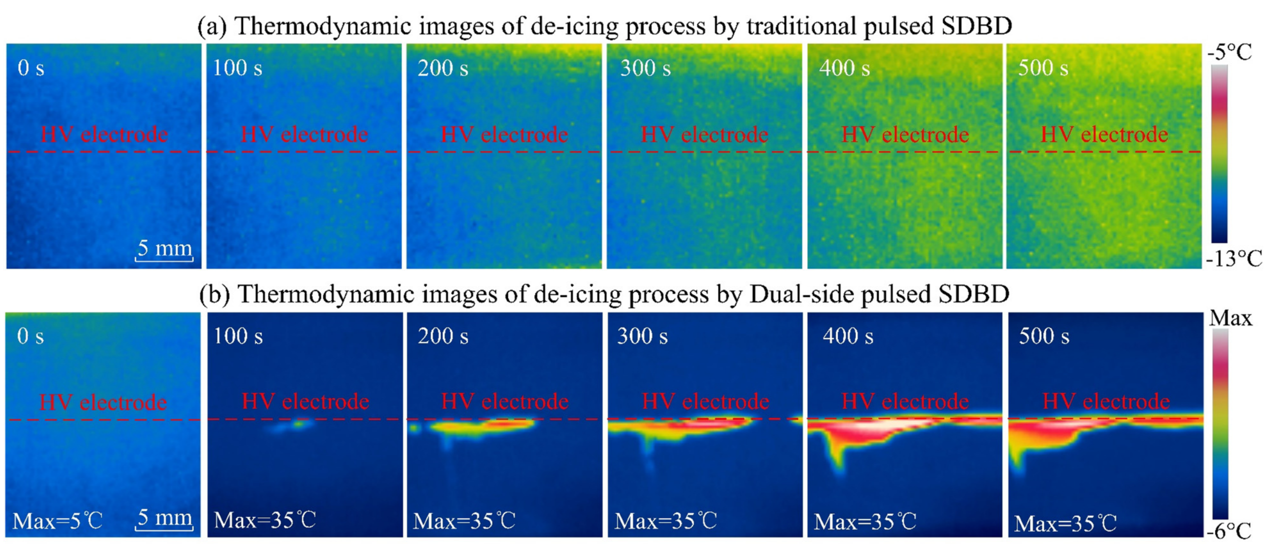

FIG. 5. Thermodynamic images during the deicing process via (a) traditional pulsed SDBD and (b) dual-side pulsed SDBD.

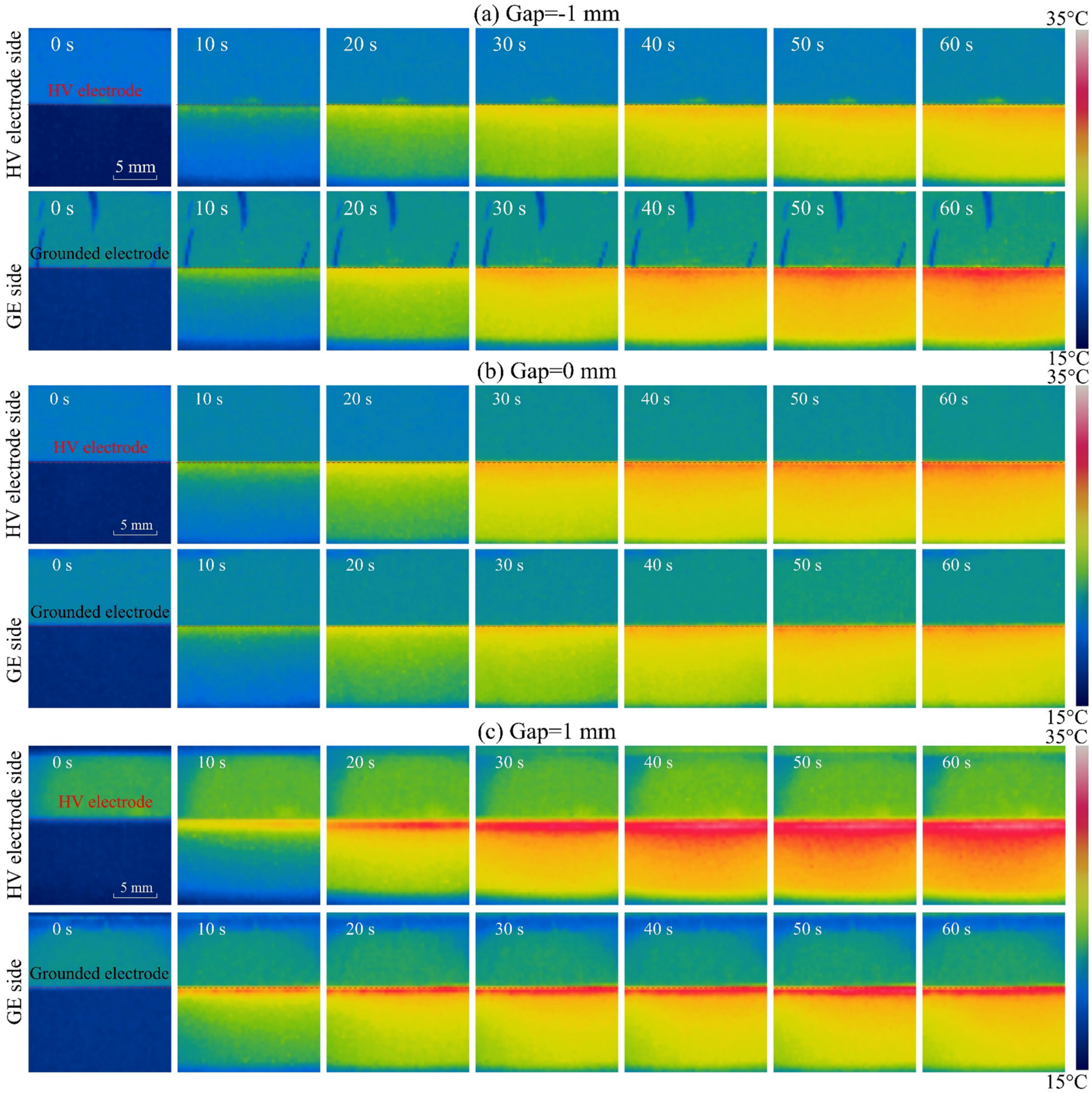

FIG. 7. Spatial-temporal evolution of surface temperature under the pulse voltage of 8 kV and pulse frequency of 1 kHz for the dual-side pulsed SDBD with the three gaps of (a) −1 mm, (b) 0 mm, and (c) 1 mm.

D. Heat distribution and discharge evolution of dual-side pulsed SDBD

In order to have a deep insight into the heat generation and distribution of the dual-side pulsed SDBD with the three gaps, a 2 D plasma fluid model is implemented to study the heat density distribution after single pulse, as shown in Fig. 9. From the results, it can be noted that the dual-side pulsed SDBD with a gap of 1 mm shows the high and large heat density on the HV electrode side. The heat generation from GE shows a similar distribution along the dielectric surface among the three different SDBD configurations. This phenomenon is agreement with experimental measurement in Fig. 7. Furthermore, a high heat density occurs around the GE, which should be favorable for the deicing through the heat conduction. The heat produced on HV electrode side is mainly caused by two discharge processes characterized with primary positive streamer and secondary negative streamer. Furthermore, the heat produced on GE side is also caused by two discharge processes, including primary negative streamer and secondary positive streamer. These two different discharge processes on HV

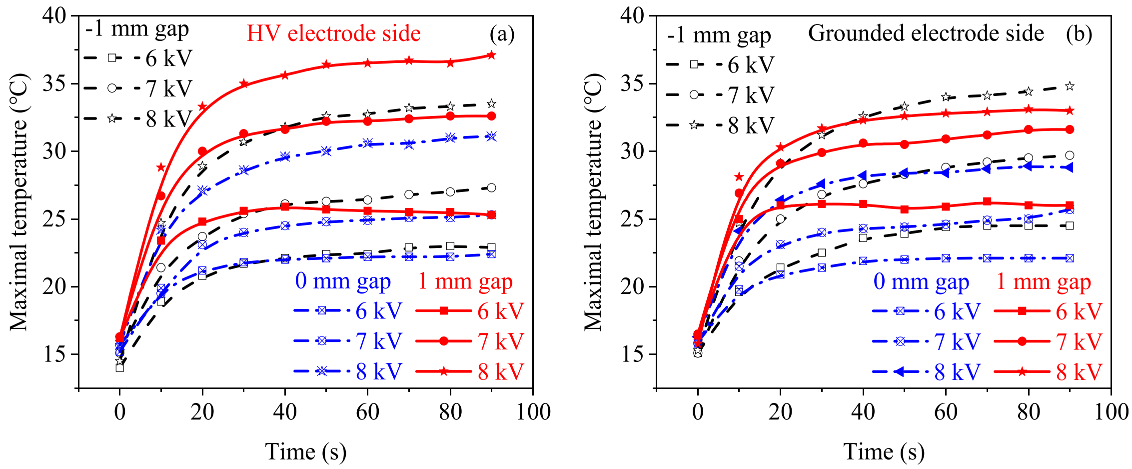

FIG. 8. Temporal evolution of maximal temperature under different applied pulse voltage for dual-side pulsed SDBD with the two dielectric sides of (a) HV electrode side and (b) GE side.

electrode and GE sides have been measured in Ref. 59, which can be demonstrated the validity of the plasma fluid model. Here, the relation between the heat density and plasma process is studied via the numerical simulation. The spatial-temporal evolution of $N_2(C^3\Pi)$ is utilized to describe the plasma process of dual-side pulsed SDBD, as shown in Fig. 10. Compared with these two discharge processes, it can be noted that plasma channel in the HV electrode region possesses a longer propagation length than that produced in the GE region. The reason is that the primary positive streamer on the HV electrode side can propagate a longer distance than that the primary negative streamer on the GE side at the rising edge of pulse. As a result, the HV electrode side possesses a long heat density and surface temperature domain. However, the secondary positive streamer produced on the GE side also occurs after the primary negative streamer. At this time, the dielectric surface accumulated with a negative charge is regarded as the cathode, and the GE is regarded as anode.[60] When the reversed electric field reaches the threshold of ionization, the secondary positive streamer is produced on the GE side.

E. Electrical characteristics during deicing process

It is a complex process for the deicing through the dual-side pulsed SDBD, which involves the plasma interactions and dynamic evolutions of four phases, including ice phase, water phase, air phase, and plasma phase. Furthermore, an actual deicing status is difficult to be monitored during the plasma deicing process in real application. It should need a series of sensors to monitor the status of covered ice, which will increase the cost of deicing. As a result, it is meaningful to determine the deicing status through the simple parameters including the electrical characteristics. Based on the relative permittivity of different medium and experimental measurements of electrical properties, the methods of single phase and double phases are developed to analyze the deicing status characteristics.[61]

1. Method of single phase analysis

A method of single phase analysis is utilized to reveal the relation between the discharge status and electrical characteristics, when the

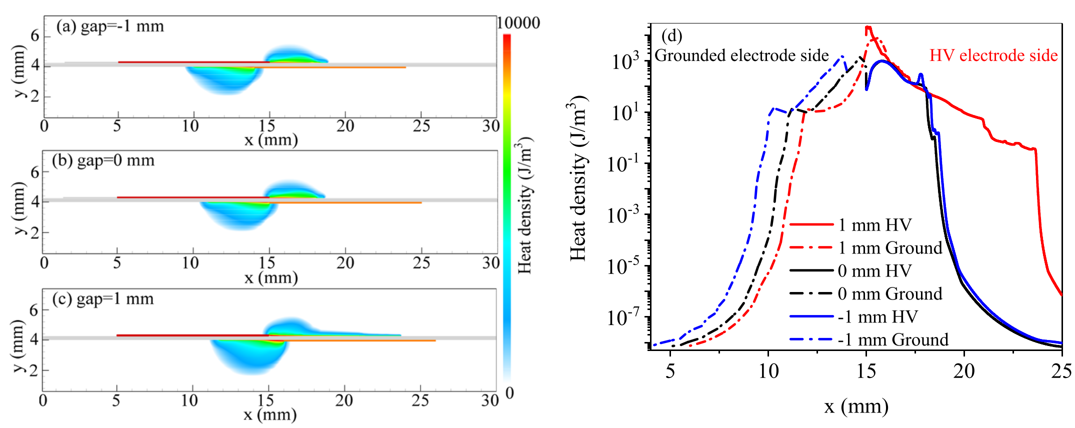

FIG. 9. Spatial distribution of heat density after single pulse discharge for the dual-side pulsed SDBD with the three gaps of (a) −1 mm, (b) 0 mm, (c) 1 mm, and (d) spatial evolution of heat density at line of y = 4.05 mm in the HV electrode side and GE side.

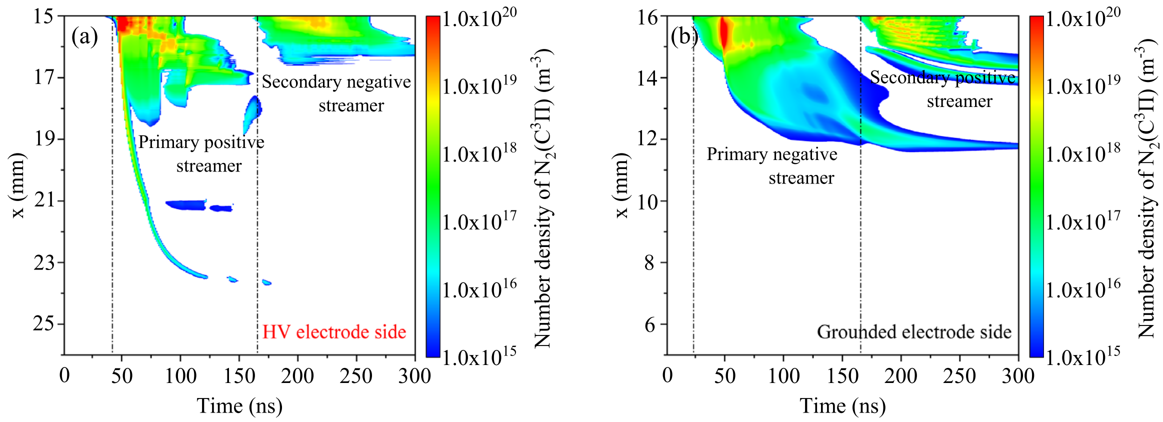

FIG. 10. Spatial-temporal evolution of $N_2(C^3\Pi)$ in the dual-side pulse SDBD with a gap of 1 mm during the discharge process for (a) HV electrode side and (b) GE side.

individual media of air, water, or ice is covered on the HV electrode side (as seen in Fig. 11). According to the typical variation of electrical characteristics under different single phase, the deicing status can be obtained through the corresponding electrical properties. The measured current and discharge power under air, ice, or water are shown in Fig. 11. It can be seen that the discharge covered with water possesses a maximal current peak among the three experimental conditions. It is due to the fact that the water has a largest relative permittivity (80), which can induce a high displacement current. However, the discharge power obtained with air has a largest value due to the reason that the plasma is generated in the two dielectric surfaces. When the HV electrode is covered with ice, the peak current and discharge power have minimal value under the different pulse voltage. The relative permittivity of ice is about 3.2,[62,63] which is lower than that of water with 80.[64,65] A high relative permittivity will induce a high electric field. The plasma is only generated on the GE side, when the ice is covered on the HV electrode side. As a result, the peak current and discharge power are low under the low relative permittivity. According to the aforementioned results, it is indicated that the evolution of discharge power and peak current can be utilized to describe the deicing status in single phase. However, the electrical characteristics are just obtained in single phase, which cannot reflect the actual deicing process including the variation of different phases. As a result, the electrical properties for the mixture of different phases should be further analyzed.

2. Method of double phase analysis

During the deicing process of dual-side pulsed SDBD, the covered glaze ice can be melted effectively. Thus, the air, water, or ice could appear on the HV electrode side. Here, the method of double phase analysis is developed to analyze the relationship between the electrical characteristics and deicing status. Plasma deicing is a gradual process, which indicates that the plasma area on the HV electrode side

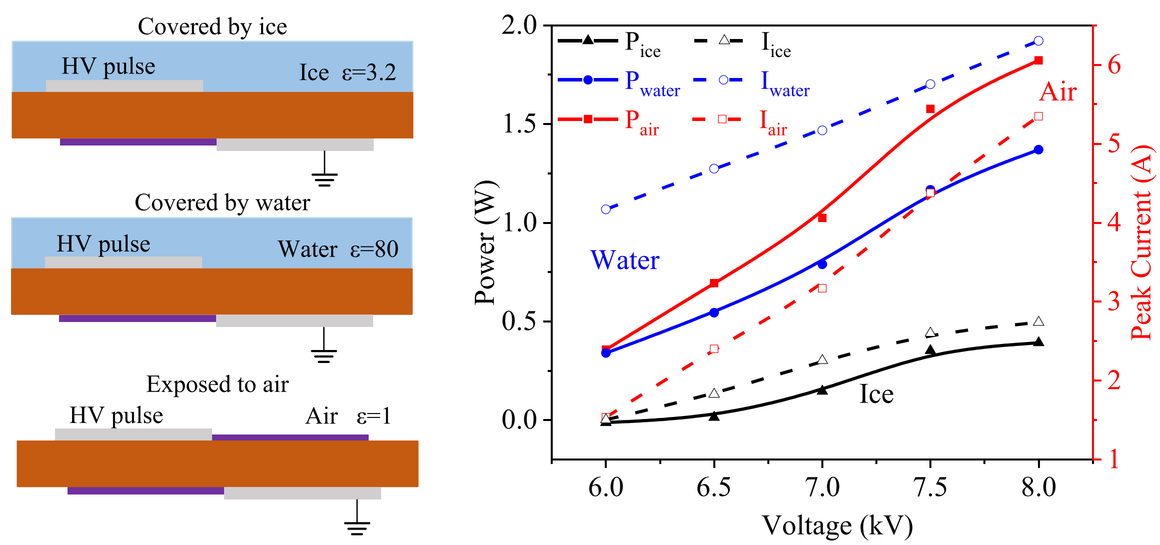

FIG. 11. Evolution of discharge power and peak current for single phase in dual-side pulsed SDBD.

increases with time. As a result, the whole discharge region of the HV electrode side can be divided into different domains, which is utilized to analyze the effect for different proportion of different phases on electrical characteristics. The proportion of air, water, and ice is assumed to be 0%, 12.5%, 25%, 50%, 75%, and 100% in double phase analysis of the whole discharge domain [as seen in Fig. 1(b)]. It can be noted that the whole model is divided into two parts. These two parts are covered with different media, resulting in three combinations, including water–ice double phases, water–air double phases, and ice–air double phases. When the HV electrode is covered with water and ice, there is no plasma produced on the HV electrode side due to the lack of gas environment. Thus, it is similar to that of the single phase which covered with water or ice. However, the different parts covered with ice or water possess the different characteristics. Because the relative permittivity of ice is different from that of water under the different frequency, the different relative permittivity induces a different polarized degree, which can produce various discharge plasma intensity. When the partial domain of HV electrode is exposed to the air, the plasma can be produced in this region. As a result, the electrical characteristics of this domain should be similar to that of the single phase of air. Figure 12 shows the evolutions of discharge power, current peak, and reactor capacity under the different proportions in double phase mixture status. For the water–air mixture, it can be noted that the discharge power decreases with the increase in water phase proportion. It is caused by the fact that the increase in water area leads to the decrease in discharge plasma area. For the current peak, it

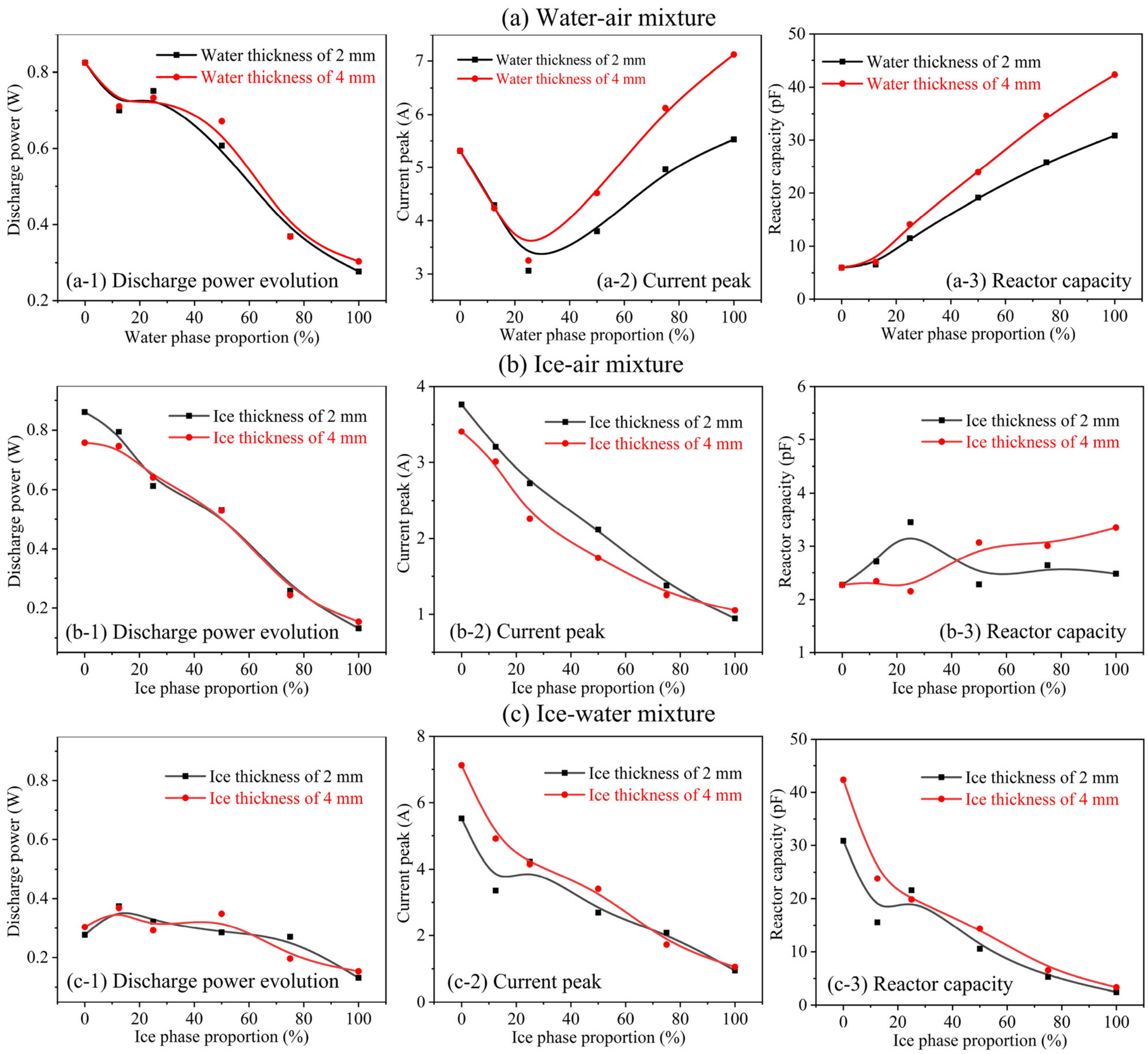

FIG. 12. Evolution of electrical characteristics under different double mixture of (a) water–air mixture, (b) ice–air mixture, and (c) ice–water mixture.

decreases before the water proportion is less than 25%. When the water proportion is greater than 25%, the current peak increases gradually [as seen in Fig. 12(a)]. The reason is that the water possesses a large relative permittivity (80), which can induce a large reactor capacitor. As a result, the reactor can produce a large displacement current when the water proportion is greater than 25%. When the water proportion is less than 25%, the plasma area plays a critical role. When some area of HV electrode is covered by the glaze ice, the discharge power also decreases with the increase in ice phase proportion in ice–air mixture status [Fig. 12(b)]. This phenomenon is also caused by the decrease in discharge plasma area. Furthermore, the current peak decreases with the increase in ice phase proportion. At this time, the reactor capacitor does not change significantly under the different ice phase proportion. The discharge plasma plays a dominant role on the current peak. When the ice and water are covered on the HV electrode side [Fig. 12(c)], the discharge power decreases slightly with the increase in ice phase proportion because more ice covered on the HV electrode side will reduce the discharge intensity in ground electrode. At this time, the measured current peak decreases with the high ice phase proportion due to the reason that the reactor capacity decreases with the increase in ice phase proportion.

F. Analysis between deicing status and electrical characteristics

According to the aforementioned single phase analysis and double phase analysis, an obvious variation of electrical characteristics for deicing process in dual-side puled SDBD can be obtained. In order to analyze the relation between the deicing status and the electrical property, a typical temporal evolution of discharge power, peak current, and maximal temperature is shown in Fig. 13. From the results, it can be seen that there are four stages during the deicing process. For the first stage, the plasma is generated in the ground electrode side, while the HV electrode is covered with glaze ice. At this time, the peak current and discharge power are unchanged, and the maximal temperature increases gradually to the ice point (0 °C). When the maximal temperature exceeds 0 °C, it transforms into second stage, which contains ice–water mixture. The covered glaze ice is melted into water through the thermal effect from the plasma in ground electrode side. At this stage, the peak current and discharge power are enhanced under the mixture of ice and water. More water covered on the HV electrode is beneficial for the generation of discharge plasma on GE side, which can induce high discharge power and current peak. Furthermore, more water covered on the HV electrode surface will possess a high reactor capacity,[66] which can produce a high displacement current. This variation is according to the aforementioned sections of water–ice mixture phase. After some water flow away from the HV electrode side, the deicing process enters the third stage, including ice, water, and air mixture. At this stage, the current peak decreases sharply because the reactor capacity decreases with the reduction of water. Moreover, the discharge power rises due to the increase in plasma region. With the increase in plasma domain, the deicing process enters fourth stage characterized with increased current peak and discharge power slightly, which is caused by the fact that the discharge area reaches a steady state.

IV. CONCLUSIONS

The deicing process and its status characteristics of dual-side pulsed SDBD are studied through the evolutions of plasma morphology, electric properties, surface temperature, and numerical simulation. The main features are as follows:

(1) When the HV electrode is covered with glaze ice, the maximal temperature of traditional pulsed SDBD is still below 0 °C during the deicing process, which indicates that it is unable to produce the plasma and remove the ice. Compared to the traditional pulsed SDBD, the maximal temperature of dual-side pulsed SDBD increases and reaches to 0 °C after the operation

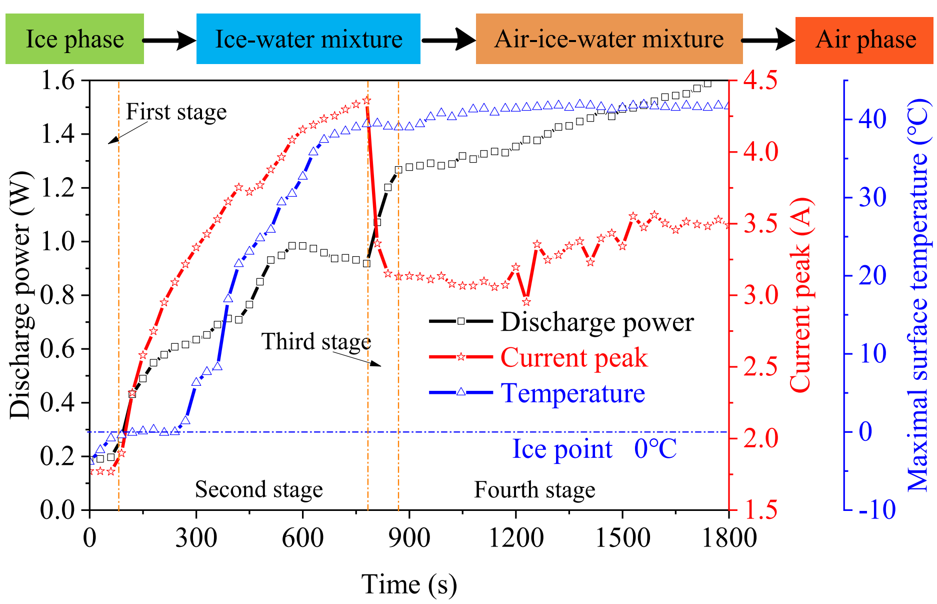

FIG. 13. Deicing status analysis by temporal evolutions of discharge power, current peak, and maximal surface temperature during the deicing process with a 2 mm thick ice.

time of 100 s, which means that it can remove the covered glaze ice effectively. The maximal temperature of the dual-side pulsed SDBD reaches 39.5 °C under the discharge time of 800 s, while the maximal temperature of traditional pulsed SDBD is still below ice point about −7.8 °C.

(2) Among the results of dual-side pulsed SDBD with the three gaps, the SDBD of 1 mm gap shows a high surface temperature and large covered area through the experiment and numerical simulation. The maximal surface temperature reaches 37.1 °C under the pulse of 8 kV after the discharge duration of 90 s. From the analysis of numerical simulation, the long primary positive streamer of 8.6 mm plays a critical role on the lager temperature region on the HV electrode side.

(3) Combining the temporal evolution of electrical characteristics and phase analysis, it indicates that there are four typical stages, including ice phase, ice–water mixture, air–ice–water mixture, and air phase in the deicing process of dual-side pulsed SDBD. The water covered on the HV electrode side induces a high reactor capacity, which can enhance the current peak through the displacement current. However, the covered glaze ice does not have a significant effect on the current peak due to the low relative permittivity. The plasma area plays a critical role on discharge power and peak current.

This work focuses on the electrical-optical properties and status characteristics of deicing process by dual-side pulsed SDBD. In the future work, the mechanism of plasma interacting with ice and water will be investigated through the experimental measurements and numerical simulation. Also, the environmental conditions of real anti-icing and deicing including gas temperature, gas velocity, and gas flow direction should be considered in the further research, which can provide references for the practical application.

ACKNOWLEDGMENTS

This work was supported by the National Natural Science Foundation of China (NSFC) (Grant Nos. 52107140, 52177130, 51877027, and 52366011) and the China Postdoctoral Science Foundation (Nos. 2021M700662 and 2022T150083).

AUTHOR DECLARATIONS

Conflict of Interest

The authors have no conflicts to disclose.

Author Contributions

Bangfa Peng: Formal analysis (lead); Visualization (equal); Writing – original draft (lead); Writing – review & editing (lead). **Jie Li:** Supervision (lead); Writing – review & editing (supporting). **Nan Jiang:** Data curation (lead); Resources (equal). **Yan Jiang:** Software (lead); Validation (equal). **Zhanqing Chen:** Methodology (equal). **Zhipeng Lei:** Resources (equal); Software (supporting). **Jiancheng Song:** Project administration (lead); Validation (supporting).

DATA AVAILABILITY

The data that support the findings of this study are available from the corresponding author upon reasonable request.

REFERENCES

[1]X. Meng, H. Hu, C. Li, A. A. Abbasi, J. Cai, and H. Hu, "Mechanism study of coupled aerodynamic and thermal effects using plasma actuation for anti-icing," Phys. Fluids **31**(3), 037103 (2019).
[2]X. Wang, J. Kou, and W. Zhang, "Unsteady aerodynamic prediction for iced airfoil based on multi-task learning," Phys. Fluids **34**(8), 087117 (2022).
[3]A. Sheidani, S. Salavatidezfouli, G. Stabile, M. Barzegar Gerdroodbary, and G. Rozza, "Assessment of icing effects on the wake shed behind a vertical axis wind turbine," Phys. Fluids **35**, 095135 (2023).
[4]C. Shinan, Q. Haifeng, S. He, and D. Huanyu, "Numerical simulation of ice shedding motion characteristic on airfoil surface," Phys. Fluids **35**, 045125 (2023).
[5]J. Chen, P. Yang, Y. Zhang, and S. Fu, "Aerodynamic prediction and roughness implementation toward ice accretion simulation," Phys. Fluids **36**, 014107 (2024).
[6]Y. Liu, C. Kolbakir, A. Y. Starikovskiy, R. Miles, and H. Hu, "An experimental study on the thermal characteristics of NS-DBD plasma actuation and application for aircraft icing mitigation," Plasma Sources Sci. Technol. **28**(1), 014001 (2019).
[7]Y. Wu, L. Dong, X. Shu, Y. Yang, P. Feng, and Q. Ran, "Recent advancements in photothermal anti-icing/deicing materials," Chem. Eng. J. **469**, 143924 (2023).
[8]K. Golovin, S. P. R. Kobaku, D. H. Lee, E. T. DiLoreto, J. M. Mabry, and A. Tuteja, "Designing durable icephobic surfaces," Sci. Adv. **2**(3), e1501496 (2016).
[9]S. K. Thomas, R. P. Cassoni, and C. D. MacArthur, "Aircraft anti-icing and de-icing techniques and modeling," J. Aircr. **33**(5), 841 (1996).
[10]S. Nijdam, J. Teunissen, and U. Ebert, "The physics of streamer discharge phenomena," Plasma Sources Sci. Technol. **29**(10), 103001 (2020).
[11]X.-F. Zhou, H.-F. Xiang, M.-H. Yang, W.-Q. Geng, and K. Liu, "Temporal evolution characteristics of the excited species in a pulsed needle-water discharge: Effect of voltage and frequency," J. Phys. D: Appl. Phys. **56**(45), 455202 (2023).
[12]N. Jiang, X. Kong, X. Lu, B. Peng, Z. Liu, J. Li, K. Shang, N. Lu, and Y. Wu, "Promoting streamer propagation, active species generation and trichloroethylene degradation using a three-electrode nanosecond pulsed sliding DBD nanosecond plasma," J. Cleaner Prod. **332**, 129998 (2022).
[13]J. Chen, H. Zong, H. Song, Y. Wu, H. Liang, and Z. Su, "Closed-loop plasma flow control of a turbulent cylinder wake flow using machine learning at Reynolds number of 28 000," Phys. Fluids **36**, 015123 (2024).
[14]A. Starikovskiy and N. Aleksandrov, "Plasma-assisted ignition and combustion," Prog. Energy Combust. Sci. **39**(1), 61–110 (2013).
[15]K. H. R. Rouwenhorst, F. Jardali, A. Bogaerts, and L. Lefferts, "From the Birkeland–Eyde process towards energy-efficient plasma-based NOX synthesis: A techno-economic analysis," Energy Environ. Sci. **14**(5), 2520–2534 (2021).
[16]Z. Wang, L. Liu, D. Liu, M. Zhu, J. Chen, J. Zhang, F. Zhang, J. Jiang, L. Guo, X. Wang, and M. Rong, "Combination of NO_x mode and O_3 mode air discharges for water activation to produce a potent disinfectant," Plasma Sources Sci. Technol. **31**(5), 05LT01 (2022).
[17]X. Deng and Z. Hou, "Thermal characteristic and spatial morphology between electrode and phase changing ice during de-icing process of dielectric barrier discharge and critical behavior of the surface charge density," Int. J. Heat Mass Transfer **190**, 122556 (2022).
[18]L. Xie, H. Liang, H. Zong, X. Liu, and Y. Li, "Multipurpose distributed dielectric-barrier-discharge plasma actuation: Icing sensing, anti-icing, and flow control in one," Phys. Fluids **34**(7), 071701 (2022).
[19]Z. Chen, C. C. Wong, and C.-Y. Wen, "Thermal effects on the performance of a nanosecond dielectric barrier discharge plasma actuator at low air pressure," Phys. Fluids **35**, 017110 (2023).
[20]W. Hui, H. Zhang, J. Wang, X. Meng, and H. Li, "Heat transfer characteristics of plasma actuation in different boundary-layer flows," Phys. Fluids **34**, 034110 (2022).
[21]B. Peng, J. He, Z. Liu, X. Yao, N. Jiang, K. Shang, N. Lu, J. Li, and Y. Wu, "Ice-breaking by three-electrode pulsed surface dielectric barrier discharge: Breakdown mode transition," J. Phys. D: Appl. Phys. **52**(50), 50LT01 (2019).
[22]S. Yang, X. Yi, Q. Guo, C. Xiao, Z. Luo, and Y. Zhou, "Novel hybrid ice protection system combining thermoelectric system and synthetic jet actuator," AIAA J. **59**(4), 1496–1500 (2020).

[23]B. Peng, N. Jiang, K. Shang, N. Lu, J. Li, and Y. Wu, "Characteristics of three-electrode pulsed surface dielectric barrier discharge: Streamer-to-spark transition and hydrodynamic expansion," J. Phys. D: Appl. Phys. 55(26), 265202 (2022).
[24]X. Meng, J. Cai, Y. Tian, X. Han, and D. Zhang, "Experimental study of anti-icing and deicing on a cylinder by DBD plasma actuation," AIAA Paper No. 2016-4019, 2016.
[25]Y. Liu, C. Kolbakir, H. Hu, and H. Hu, "A comparison study on the thermal effects in DBD plasma actuation and electrical heating for aircraft icing mitigation," Int. J. Heat Mass Transfer 124, 319–330 (2018).
[26]Y. Liu, C. Kolbakir, H. Hu, X. Meng, and H. Hu, "An experimental study on the thermal effects of duty-cycled plasma actuation pertinent to aircraft icing mitigation," Int. J. Heat Mass Transfer 136, 864–876 (2019).
[27]C. Kolbakir, Y. Liu, H. Hu, A. Starikovskiy, and R. B. Miles, "An experimental investigation on the thermal effects of NS-DBD and AC-DBD plasma actuators for aircraft icing mitigation," AIAA Paper No. 2018-0164, 2018.
[28]B. Wei, Y. Wu, H. Liang, Y. Zhu, J. Chen, G. Zhao, H. Song, M. Jia, and H. Xu, "SDBD based plasma anti-icing: A stream-wise plasma heat knife configuration and criteria energy analysis," Int. J. Heat Mass Transfer 138, 163–172 (2019).
[29]X. Zheng, H. Song, D. Bian, H. Liang, H. Zong, Z. Huang, Y. Wang, and W. Xu, "A hybrid plasma de-icing actuator by using SiC hydrophobic coating-based quartz glass as barrier dielectric," J. Phys. D: Appl. Phys. 54, 375202 (2021).
[30]M. Lindner, A. V. Pipa, N. Karpen, R. Hink, D. Berndt, R. Foest, E. Bonaccurso, R. Weichwald, A. Friedberger, R. Caspari, R. Brandenburg, and R. Schreiner, "Icing mitigation by MEMS-fabricated surface dielectric barrier discharge," Appl. Sci. 11, 11106 (2021).
[31]Y. Zhong, Z. Jin, M. Chen, and Z. Yang, "An experimental investigation of the thermal effects in AC-DBD plasma actuator on the melting process of an ice bead," Exp. Therm. Fluid Sci. 147, 110950 (2023).
[32]B. Wei, Y. Wu, H. Liang, J. Chen, G. Zhao, M. Tian, and H. Xu, "Performance and mechanism analysis of nanosecond pulsed surface dielectric barrier discharge based plasma deicer," Phys. Fluids 31, 091701 (2019).
[33]Y. Zhu, Y. Wu, B. Wei, H. Xu, H. Liang, M. Jia, H. Song, and Y. Li, "Nanosecond-pulsed dielectric barrier discharge-based plasma-assisted anti-icing: Modeling and mechanism analysis," J. Phys. D: Appl. Phys. 53, 145205 (2020).
[34]S. Ihara and C. Yamabe, "Breaking of ice using pulsed power," Jpn. J. Appl. Phys., Part 1 43(8A), 5528–5532 (2004).
[35]T. Gao, Z. Luo, Y. Zhou, Z. Liu, W. Peng, P. Cheng, and X. Deng, "Novel deicing method based on plasma synthetic jet actuator," AIAA J. 58(9), 4181–4188 (2020).
[36]T. Gao, Z. Luo, Y. Zhou, S. Yang, W. Peng, X. Deng, and P. Cheng, "Experimental investigation on ice-breaking performance of a novel plasma striker," Chin. J. Aeronaut. 35(1), 307–317 (2022).
[37]Y. Han, J. Palacios, and S. Schmitz, "Scaled ice accretion experiments on a rotating wind turbine blade," J. Wind Eng. Ind. Aerodyn. 109, 55–67 (2012).
[38]N. Sakakibara and K. Terashima, "Generation of H_2O-ice dielectric barrier discharge for the development of novel cryogenic reaction fields," J. Phys. D: Appl. Phys. 50(22), 22LT01 (2017).
[39]J. Kruszelnicki, R. Ma, and M. J. Kushner, "Propagation of atmospheric pressure plasmas through interconnected pores in dielectric materials," J. Appl. Phys. 129(14), 143302 (2021).
[40]C. Li, J. Teunissen, M. Nool, W. Hundsdorfer, and U. Ebert, "A comparison of 3D particle, fluid and hybrid simulations for negative streamers," Plasma Sources Sci. Technol. 21(5), 055019 (2012).
[41]W. Ning, J. Lai, J. Kruszelnicki, J. E. Foster, D. Dai, and M. J. Kushner, "Propagation of positive discharges in an air bubble having an embedded water droplet," Plasma Sources Sci. Technol. 30(1), 015005 (2021).
[42]A. Komuro, T. Ryu, A. Yoshino, T. Namihira, D. Wang, and R. Ono, "Streamer propagation in atmospheric-pressure air: Effect of the pulse voltage rise rate from 0.1 to 100 kV/ns and streamer inception voltage," J. Phys. D: Appl. Phys. 54, 364004 (2021).
[43]W. Wang, H.-H. Kim, K. Van Laer, and A. Bogaerts, "Streamer propagation in a packed bed plasma reactor for plasma catalysis applications," Chem. Eng. J. 334, 2467–2479 (2018).
[44]V. R. Soloviev, E. M. Anokhin, and N. L. Aleksandrov, "Spatial distribution of radiation emitted by pulsed surface dielectric barrier discharge in air," Plasma Sources Sci. Technol. 29(3), 035006 (2020).
[45]Y. Zhu, X. Chen, Y. Wu, and S. Starikovskaia, *PASSKEy code [software]* (Science and Technology of Plasma Dynamics Laboratory, China and Laboratoire de Physique des Plasmas, 2021), see http://www.plasma-tech.net/parser/passkey/.
[46]Y. Zhu, X. Chen, Y. Wu, J. Hao, X. Ma, P. Lu, and P. Tardiveau, "Simulation of ionization-wave discharges: A direct comparison between the fluid model and E-FISH measurements," Plasma Sources Sci. Technol. 30(7), 075025 (2021).
[47]X. Chen, Y. Zhu, Y. Wu, J. Hao, X. Ma, and P. Lu, "Numerical investigations of nanosecond surface streamers at elevated pressure," Plasma Sources Sci. Technol. 30, 075008 (2021).
[48]A. Bourdon, V. P. Pasko, N. Y. Liu, S. Célestin, P. Ségur, and E. Marode, "Efficient models for photoionization produced by non-thermal gas discharges in air based on radiative transfer and the Helmholtz equations," Plasma Sources Sci. Technol. 16(3), 656–678 (2007).
[49]A. V. Phelps and L. C. Pitchford, "Anisotropic scattering of electrons by N2 and its effect on electron transport," Phys. Rev. A 31(5), 2932–2949 (1985).
[50]S. A. Lawton and A. V. Phelps, "Excitation of the $b^1\Sigma+$ g state of O_2 by low energy electrons," J. Chem. Phys. 69(3), 1055–1068 (1978).
[51]N. Popov, "Fast gas heating in a nitrogen–oxygen discharge plasma: I. Kinetic mechanism," J. Phys. D: Appl. Phys. 44(28), 285201 (2011).
[52]I. Kossyi, A. Y. Kostinsky, A. Matveyev, and V. Silakov, "Kinetic scheme of the non-equilibrium discharge in nitrogen-oxygen mixtures," Plasma Sources Sci. Technol. 1(3), 207–220 (1992).
[53]S. Pancheshnyi, M. Nudnova, and A. Starikovskii, "Development of a cathode-directed streamer discharge in air at different pressures: Experiment and comparison with direct numerical simulation," Phys. Rev. E 71(1), 016407 (2005).
[54]J. Poggie, I. Adamovich, N. Bisek, and M. Nishihara, "Numerical simulation of nanosecond-pulse electrical discharges," Plasma Sources Sci. Technol. 22(1), 015001 (2012).
[55]G. Hagelaar and L. Pitchford, "Solving the Boltzmann equation to obtain electron transport coefficients and rate coefficients for fluid models," Plasma Sources Sci. Technol. 14(4), 722–733 (2005).
[56]B. Huang, C. Zhang, W. Zhu, X. Lu, and T. Shao, "Ionization waves in nanosecond pulsed atmospheric pressure plasma jets in argon," High Voltage 6(4), 665–673 (2021).
[57]S. B. Leonov, I. V. Adamovich, and V. R. Soloviev, "Dynamics of near-surface electric discharges and mechanisms of their interaction with the airflow," Plasma Sources Sci. Technol. 25(6), 063001 (2016).
[58]R. Tirumala, N. Benard, E. Moreau, M. Fenot, G. Lalizel, and E. Dorignac, "Temperature characterization of dielectric barrier discharge actuators: Influence of electrical and geometric parameters," J. Phys. D: Appl. Phys. 47(25), 255203 (2014).
[59]Y. Jiang, B. Peng, Z. Liu, N. Jiang, N. Lu, K. Shang, and J. Li, "Characteristic studies on positive and negative streamers of double-sided pulsed surface dielectric barrier discharge," Plasma Sci. Technol. 24, 044005 (2022).
[60]V. R. Soloviev, V. M. Krivtsov, S. A. Shcherbanev, and S. M. Starikovskaia, "Evolution of nanosecond surface dielectric barrier discharge for negative polarity of a voltage pulse," Plasma Sources Sci. Technol. 26, 014001 (2016).
[61]M. Abdollahzadeh, F. Rodrigues, and J. C. Pascoa, "Simultaneous ice detection and removal based on dielectric barrier discharge actuators," Sens. Actuators, A 315, 112361 (2020).
[62]K. Watanabe and T. Wake, "Measurement of unfrozen water content and relative permittivity of frozen unsaturated soil using NMR and TDR," Cold Reg. Sci. Technol. 59, 34–41 (2009).
[63]M. A. Hilhorst, C. Dirksen, F. W. H. Kampers, and R. A. Feddes, "Dielectric relaxation of bound water versus soil matric pressure," Soil Sci. Soc. Am. J. 65, 311–314 (2001).
[64]G. C. Topp, S. Zegelin, and I. White, "Impacts of the real and imaginary components of relative permittivity on time domain reflectometry measurements in soils," Soil Sci. Soc. Am. J. 64, 1244–1252 (2000).
[65]D. A. Robinson, C. M. K. Gardner, and J. D. Cooper, "Measurement of relative permittivity in sandy soils using TDR, capacitance and theta probes: Comparison, including the effects of bulk soil electrical conductivity," J. Hydrol. 223, 198–211 (1999).
[66]M. Abdollahzadeh, F. Rodrigues, J. Nunes-Pereira, J. C. Pascoa, and L. Pires, "Parametric optimization of surface dielectric barrier discharge actuators for ice sensing application," Sens. Actuators, A 335, 113391 (2022).